KSME Journal, Vol. 6, No. 2, pp. 169~177, 1992

OFF-DESIGN SOLUTIONS OF HYPERSONIC FLOWS PAST ELLIPTIC-CONE DERIVED WAVERIDERS

Bok-hyun Yoon

(Received July 5, 1992)

A comprehensive study for the inviscid numerical calculation on the hypersonic flows past a class of elliptic-cone derived waveriders at both on-design and off-design conditions has been accomplished by the author. The portion of the on-design solutions has been reported already. In this paper, numerical results for the hypersonic flows at various off-design conditions are presented and their flowfield characteristics are analyzed as well. At Mach numbers greater than the design condition, a lambda-shock configuration develops near the tip of the compression surface. At negative angles of attack, other complicated shock patterns occur near the leading-edge tip. These heretofore unknown flow patterns show the power and utility of CFD for investigating novel hypersonic configurations such as waveriders.

Key Words: Waverider, Hypersonic Flow, CFD, Shock Wave, Expansion Wave, Off-Design Solution, λ-Shock

NOMENCLATURE

e	: Internal energy per unit mass
E_t	: Total energy
J	: Jacobian
M_∞	: Freestream Mach number
$\hat{n}$	: Outward unit normal vector
p	: Pressure
P	: Source term of Poisson's equation for η
Q	: Source term of Poisson's equation for ζ
$\vec{r}$	: Position vector
S	: Arc length
t	: Time
T	: Temperature
$\bar{U}$	: Conservative variable column matrix
$\vec{V}_\infty$	: Freestream velocity
a,b	: Exponential of P and Q source terms of Poisson's equation
w	: Weight function
$\hat{E}\ \hat{F}\ \hat{G}$	: Flows in ξ, η, and ζ-directions
$\bar{E}\ \bar{F}\ \bar{G}$	: Cartesian fluxes in the x, y, and z-directions
k, l, n	: Indices for η, ζ, and time
u, v, w	: Cartesian velocity components
$\bar{U},\bar{V},\bar{W}$	: Contravariant velocity components
$p(\xi),q(\xi)$	: Components of P and Q source terms of Poisson's equation
x, y, z	: Cartesian coordinates
α	: Angle of attack
β	: Angle of yaw
δ	: Half cone angle
γ	: Ratio of specific heats
ϕ	: Azimuthal angle
θ	: Conical angle
ρ	: Density
ξ, η, ζ	: Generalized curvilinear coordinates
r, θ, ϕ	: Spherical coordinates

*Department of Mechanical Engineering, College of Engineering, Mokpo National University, #61 Dorim-ri, Chyung ge-myun, Muan-gun, Cheonnam, 534-729 Republic of Korea

1. INTRODUCTION

As the study for hypersonic vehicles progresses in the aerospace science field, the waverider has been highlighted with deep concern for recent years. In order to consider any practical use of the waverider such as the forebody of an aerospace plane, it is important that its off-design performance should be well understood. The underlying concept of waverider is that the on-design conditons are easy to calculate. On the other hand, the off-design conditions, at which we expect quite complicated flow patterns, are neither well understood nor fully analyzed in detail. Under the circumstances, the study of hypersonic flows past waverider at off-design conditions is a quite challenging task.

For the analysis of the problem three approaches may be taken into consideration. Firstly, the study for the off-design conditions by means of analytical approach is nearly impossible at this point. This method has been limited to on-design conditions only. Accordingly, for that purpose experimental approach (Rasmussen, Jischke, Daniel, 1982, Jischke, Rasmussen, Daniel, 1983) had played a major role. Its drawback is high cost to run a hypersonic wind tunnel and to access or purchase such high-priced facilities for experiment. Besides, it would be another problem to set up high altitude atmospheric conditions at which space-crafts are supposed to fly.

As in other research fields, numerical analysis becomes a more powerful tool in the fluid dynamics area too. Nevertheless, researches on hypersonic flows past waveriders by numerical analysis have been very rare up to now, possibly because of the intrinsic geometrical and physical singularities of the waverider problem. Jones(Jones, 1986) used the full potential method for numerical calculation for the first time to solve supersonic flows past waveriders. However, his results are neither accurate nor adequate for high supersonic flow regime because of his simplified equations. For example,

the inaccuracy increases, as the angle of attack becomes larger, which indicates more hypersonic flow feature at such off-design conditions. In short, his analysis is not meaningful in hypersonic flow regions. Recently, some papers (Long, 1990, Jones, Dougherty, 1990, Lia, Issac, Miles, 1990) by CFD (Computational Fluid Dynamics) method were published, just as the author's comprehensive numerical study for the waverider flowfields was completed, as mentioned in the previous report(Yoon, 1992). One paper is limited to a narrow range of off-design conditions and the other paper calculates for small off-design data points. As an instance, Long's paper (Long, 1990) reports only two off-design data points for the lift to drag ratio with 29×25 mesh. These are obviously insufficient for checking both the accuracy and the trend, and also for plotting a graph. Furthermore, none of them deals with the detailed flow patterns such as the shock structure near the leading edge and an imbedded shock arising from the different angle of attack from the designed value.

In this investigation, we deal with the extensive range of off-design conditions with typical grid 83×41 mesh. That is, the freestream Mach number ranges 3 to 10 and the angle of attack ranges -12° to $+10^{\circ}$. This does mean more than the simple extension of the off-design range. This implies that various obstacles for numerical convergence, which is the main difficulty in this problem, were removed to such an extent. This may be confirmed from Jones' report (Jones, Dougherty, 1990) that the PNS code, that was the very code on which this research was done successfully, breaks down for bodies with sharp leading edges like waveriders. The aim of this paper is to analyze some hypersonic flow characteristics at various off-design conditions, some of which are neither observed nor analyzed heretofore. These include the lambda-shock near the leading edge of the investigated waverider, other complicated shock strcutures, and flowfield comparisons with the freestream Mach number and/or angle of attack varying as parameters.

2. PROBLEM FEATURES IN NUMERICAL ANALYSIS

The numerical calculation of flows past waverideors involves difficulties that fall into at least three categories which are somewhat interrelated. The first category is associated with the singular nature of the waverider shape at the sharp leading edge. The second category is associated with the large gradients in the flow arising from the bow shock wave, the large gradients near the sharp leading edge especially when the freestream Mach number is slightly less than the design Mach number, and possibly large gradients arising from vortical layers. The third category is the numerical algorithm itself, including the implementation of the wall boundary condition.

The upper surface of the elliptic-cone derived waverider is a flat delta-shaped surface that intersects the lower curved compression surface along a straight line that forms the sharp leading edge of the waverider. The singular behavior of this leading edge presents difficulties in constructing smoothly-varying grid cells near the leading edge. Some grid construction schemes are tested : an O-type grid, a fan-type grid, and an adaptive grid. If the grid is skewed to a certain degree or if the grid cell volumes change very rapidly, the numerical integration will results in divergence. An adaptive grid may be used to improve the resolution and accuracy for capturing shocks. This, however, would yield grid skewness for both the sharp leading edge region and the bow shock region. As a test case, an adaptive grid was used with the hope for an improved shock structure, but it did not lead to a successful converged solution. It should be noted here that a very slightly skewed grid introduced by the adaptiveness could be the source of divergence in an attempt to numerically integrate governing equations. This tells that the convergence of the numerical integration is severely influenced by the grid structure near the tip. Among various methods for gird generation, an elliptic grid generation is adopted, because it produces a very smooth gird. Although the overall geometry of the waverider seems to be simple, a lot of effort should be exerted to get a desirable gird structure especially near the tip. For that purpose Roberts' stretching (Anderson, Tannehill, Pletcher, 1984), Sorenson's method (Sorenson, 1980), and Anderson's adaptive grid method (Anderson, 1987) are adopted.

This paper deals with the flowfields at off-design conditions which occur when either the freestream Mach number or angle of attack is different from the related design value. The effect of the second difficulty stated earlier will be worse, as the Mach number and/or the angle of attack increase, where the flow becomes more rotational and thus exhibit more distinguished features of hypersonic flow with a large number of hypersonic similarity parameter. Obviously this would place restrictions on the magnitude of both Mach number and the angle of attack for numerical calculations.

Numerous numerical algorithms and methods can be considered for numerical integration and discretizing the Euler equations which are used in this study. In this investigation, Lawrence's STARS3D code based on his algorithm, which is a steady version of Roe's approximate Riemann solver (Roe, 1981) and is in the class of upwind schemes, is utilized to solve the hypersonic flows past elliptic-cone waverders. The upwind schemes can be classified into two categories ; Flux Vector Splitting(FVS) (van Leer, 1982) and Flux Difference Splitting(FDS). The FVS divides any flux into the positive and negative parts first according to the sign of its relevant eigenvalues and then discretizes them by using one-sided differences. The FDS determines a flux difference for two corresponding cell interfaces first and then discretizes the flux difference according to the relevant eigenvalues. Lawrence et al. (Lawrence, Tannehill and Chaussee, 1986) applied a Total Variation Diminishing(TVD) (Yee, Harten, 1987, Harten, 1983) schemes of Chakravarthy et al. (Chakravarthy, Osher, 1985, Chakravarthy, Szema, Goldberg, Gorski and Osher, 1985) to the PNS equations to develop an algorithm which is in the category of the FDS. The TVD schemes have attracted much attention in the field of hypersonic flows, since they have some desirable properties associated with the handling of discontinuities like a shock in view of the stability and built-in dissipation. This algorithm uses the Finite Volume Method(FVM) to discretize the governing equations and an Alternating Directional Implicit method to integrate in space. The FVM, which is acquiring popularity recently over the conventional Finite Difference Method, is reported to have some advantages for the problems with irregular boundaries. In order to calculate inviscid flows, which were only possible for this problem with this code, the option for an inviscid flow was used.

3. GOVERNING EQUATIONS

The steady Euler equations which are hyperbolized, are numerically integrated for the computation. In this section governing equations with initial and boundary conditions for the numerical integration are presented.

3.1 Governing Equations in Cartesian Coordinates

The unsteady Euler equations without source terms can be written in a strong conservation-law form in a Cartesian coordinate system ($x_i : x, y, z$) as

$$\frac{\partial \bar{U}}{\partial t}+\sum_{i=1}^{3}\frac{\partial \bar{E}^i}{\partial x_i}=0 \quad (\bar{E}^i : \bar{E}, \bar{F}, \bar{G}) \tag{1}$$

where

$$\bar{U}=\{\rho, \rho u, \rho v, \rho w, E_t\}^T$$

$$\bar{E}^i=\begin{Bmatrix}\rho u_i \\ \rho u_i u+\delta_{i1}p \\ \rho u_i v+\delta_{i2}p \\ \rho u_i w+\delta_{i3}p \\ (E_t+p)\,u_i\end{Bmatrix}$$

$$E_t=\rho\left[e+\frac{1}{2}(u^2+v^2+w^2)\right]$$

where u_i are Cartesian velocity components (u, v, w), e is internal energy per unit mass, and δ_{ij} denotes the Kronecker delta function. For simplicity the ideal gas model is used here.

$$p=(\gamma-1)\,\rho e=\frac{1}{\gamma M_\infty^2}\rho T \tag{2}$$

The above equation has been nondimensionalized by taking the freestream values as reference parameters.

3.2 Governing Equations in Generalized Curvilinear Coordinates

The Euler equations in a generalized curvilinear coordinate system can be obtained through the following transformation

$$\xi^i=\xi^i(x, y, z), \quad (\xi^i : \xi, \eta, \zeta), \quad i=1, 2, 3, \tag{3}$$

where $\xi(=\xi^1)$ is taken as the radial direction. The $\eta(=\xi^2)$ is in the crosswise direction and $\zeta(=\xi^3)$ is in the normal direction to the waverider body wall. These coordinates will be generated numerically. The η and ζ coordinates are orthogonal at the body boundary but not for the leading edge neighborhood and the rest of the flowfield. In case that the ξ and η coordinates are taken to be fixed at the body wall, the generalized coordinates are called to be body-fitted coordinates. If we utilize the chain rule, the governing equations in a new coordinate system can be expressed in the strong conservation-law form again (Anderson, Tannehill, Pletcher, 1984),

$$\frac{\partial \hat{U}}{\partial t}+\sum_{i=1}^{3}\frac{\partial \hat{E}^i}{\partial \xi^i}=0 \quad (\hat{E}^i : \hat{E}, \hat{F}, \hat{G}) \tag{4}$$

where

$$\hat{U}=\frac{\bar{U}}{J} \tag{5}$$

$$\begin{Bmatrix}\hat{E} \\ \hat{F} \\ \hat{G}\end{Bmatrix}=\frac{1}{J}[A]\begin{Bmatrix}\bar{E} \\ \bar{F} \\ \bar{G}\end{Bmatrix} \tag{6}$$

where $[A]$ is defined by

$$[A]\equiv\begin{bmatrix}\xi_x & \xi_y & \xi_z \\ \eta_x & \eta_y & \eta_z \\ \zeta_x & \zeta_y & \zeta_z\end{bmatrix}$$

and the Jacobian J is defined by the determinant of $[A]$ as

$$J\equiv|A|\equiv\frac{\partial(\xi, \eta, \zeta)}{\partial(x, y, z)}$$

From Eq. (6), we can see that all the information for the fluxes of Cartesian coordinates and the flows of generalized coordinates are exchanged by means of the metrics and the Jacobian. It is to be noted here that the metrics appear in a special form such that they are divided by the Jacobian. The metrics in this form, as well as the Jacobian, have geometrical meanings. The Jacobian is equal to the inverse of the cell volume and the metrics combined with the Jacobian are area element vectors. Thus, once an appropriate grid is generated, both the metrics and the Jacobian can be determined from the geometric configuration of the grid. Therefore, the explicit form of the transformation function is not necessary at all.

3.3 Steady Hyperbolic Equations

In this study we use the steady Euler equations which are obtained from Eq. (5). They are written as

$$\frac{\partial \hat{E}}{\partial \xi}+\frac{\partial \hat{F}}{\partial \eta}+\frac{\partial \hat{G}}{\partial \zeta}=0 \tag{7}$$

To numerically integrate the governing equations in space they are to be of a hyperbolic type. The steady Euler equations become hyperbolic in the ξ direction, if we impose a restriction such that the eigenvalues of the pertinent flux Jacobian matrices ($\partial\hat{F}/\partial\hat{E}$, $\partial\hat{G}/\partial\hat{E}$) are real (Warming, Beam, Hyett, 1975). The restriction requires supersonic inviscid flow in the streamwise direction everywhere. Fortunately, the waverider problem investigated here has such a characteristic except for the case with a very high angle of attack. That is, the flow speed past waveriders for a mild angle of attack is expected to be supersonic in the streamwise direction for the whole flow region. However, this would not be the case, if the angle of attack becomes such large that so called stalling phenomenon occurs. Thus we can use the steady equations which need space marching technique. In this connection the ξ coordinate in the steady equations plays the role of the time variable in the unsteady equations.

3.4 Initial Conditions

To start the numerical integration of the Euler equations by space marching, the initial flow values at a starting point of ξ must be specified. Since the waverider has sharp leading edges and there is no inviscid subsonic region for a mild angle of attack, the supersonic freestream values can be used as initial conditions (ICs) in the numerical integration of hyperbolized governing equations. Even though the final form of the equations is expressed in the body-fitted coordinates to fit the special geometry of the waverider, the imposition of ICs for the velocity can be achieved by the utilization of the Cartesian velocity components. It is to be noted Cartesian components are still kept even in the equations expressed in the body-fitted coordinates. The initial velocity components are

$$u_{k,l}^1=V_\infty\cos\alpha, \quad v_{k,l}^1=V_\infty\sin\alpha, \quad w_{k,l}^1=0 \tag{8}$$

If necessary, the effects of the angles of yaw β may be implemented in this stage. For a special case without angles of attack and yaw where the freestream flow is in the x direction, the only nonvanishing velocity component is $u_{k,l}^1=V_\infty$. For the other flow variables such as pressure, density, and temperature, we use freestream values. The initial converged solution is sought at the position $x=0.05$, where the step-back procedure is taken until we meet any

given criterion. Since we deal with the inviscid problem only and thus the flow is conical, we don't need to integrate further downstream. The reason for the above assertion is that even for off-design conditions there is no characteristic length scale, which is the basic feature of any conical flow, and thus the flow remains still conical, since the body is conical.

3.5 Boundary Conditions

The boudnary conditions(BCs) without yaw ($\beta=0$) are composed of three parts as shown in Fig. 1 the far-field away from the bow shock, the upper and lower parts of the symmetry plane, and the body wall. For the case with angle of yaw, the symmetry condition cannot be used. In that case the whole flow region must be included in the calculation instead of the half domain with the periodic boundary condition.

Far-Field :

In a supersonic flow the flow downstream of a shock does not influence the upstream flow. Thus we can use the freestream values for the region which is far away from an expected bow shock located around the lower portion of a waverider. The outer boundary values (denoted by l_{max}) are set equal to those of the freestream as

$$\bar{U}_{l_{max}}=\bar{U}_{freestream} \tag{9}$$

When the angle of attack is such that an expansion wave exists above the waverider, the far-field condition must be imposed outside the Mach cone emanating from the apex of the waverider.

Symmetry Plane :

The waverider configuration studied in this work is symmetric about the plane $z=0$ and the flow around it will be also symmetric as long as its symmetry plane is aligned with the freestream flow direction ($\beta=0$). To impose this condition two additional neighboring grid points are necessary across both the upper and lower symmetry planes, since the numerical algorithm used is the second order in the crosswise directions. Let

$$X=\begin{bmatrix}1&0&0&0&0\\0&1&0&0&0\\0&0&1&0&0\\0&0&0&-1&0\\0&0&0&0&1\end{bmatrix} \tag{10}$$

then

$$\bar{U}_{k=1}=X\bar{U}_{k=4},\quad \bar{U}_{k=kmax+2}=X\bar{U}_{k=kmax-1}$$
$$\bar{U}_{k=2}=X\bar{U}_{k=3},\quad \bar{U}_{k=kmax+1}=X\bar{U}_{k=kmax} \tag{11}$$

Here the -1 in X plays the role of changing the sign of w across the symmetry plane.

Wall :

Since the finite-volume method is used, the wall surface is composed of cell interfaces obtained by the primary grids. Thus, fluxes instead of flow variables should be specified at the wall for imposing the boundary condition. For inviscid flow the contravariant velocity $\tilde{W}$ in the ζ-direction is zero. That is,

$$\vec{V}\cdot\hat{n}=0,\ \Rightarrow \tilde{W}\equiv\frac{\zeta_x}{J}u+\frac{\zeta_y}{J}v+\frac{\zeta_z}{J}w=0 \tag{12}$$

where

$$\hat{n}=\frac{\nabla\zeta}{|\nabla\zeta|} \tag{13}$$

As a consequence, all the inviscid normal fluxes to the wall vanish except for the pressure term.

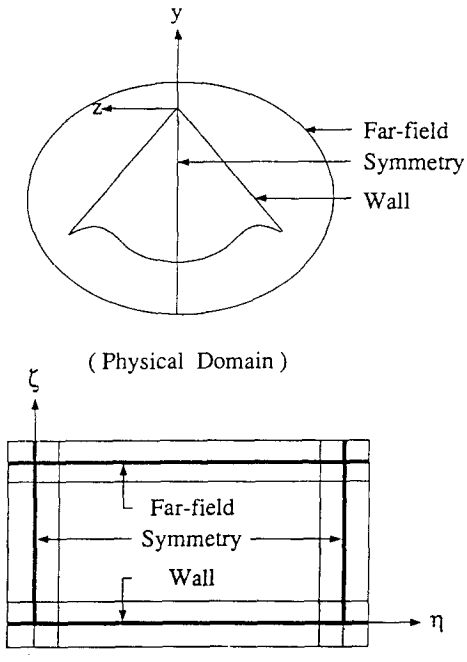

Fig. 1 Boundary conditions

4. GRID GENERATION

It is true that for general use there exist nice grid generating codes such as GRAPE(Sorenson, 1980) and EAGLE (Thompson, Lijewski, Gatlin, 1989). However, for a special problem as in the hypersonic waverider flow problem it would be more desirable to write a special grid generating code. The reason for that is that the elliptic-cone waverider studied here has a geometrical singularity and thus we need the capability of good grid control which eventually affect the convergence of numerical calculations. In order to capture a bow shock more accurately we may utilize an adaptive grid. To get a more desirable grid structure near the tip the boundary points are redistributed by means of a stretching function.

4.1 Elliptic Grid Generation

The set of equations for 2-D elliptic grid generation is

$$\alpha z_{\eta\eta}-2\beta z_{\eta\zeta}+\gamma z_{\zeta\zeta}=-\frac{1}{J^2}(Pz_\eta+Qz_\varphi) \tag{14}$$

$$\alpha y_{\eta\eta}-2\beta y_{\eta\zeta}+\gamma y_{\zeta\zeta}=-\frac{1}{J^2}(Py_\eta+Qy_\zeta) \tag{15}$$

where

$$\alpha\equiv z_\zeta^2+y_\zeta^2,\quad \beta\equiv z_\eta z_\zeta+y_\eta y_\zeta,\quad \gamma\equiv z_\eta^2+y_\eta^2 \tag{16}$$

and the Jacobian J is defined as

$$J\equiv\frac{\partial(\eta,\zeta)}{\partial(z,y)} \tag{17}$$

4.2 Control Functions

In determining control functions two factors are taken into account. One is grid control near the wall and the other is an adaptive grid. In this study the above two effects are com-

bined together as

$$P \equiv P_W + P_A, \quad Q \equiv Q_W + Q_A \tag{18}$$

where the subscript $_W$ stands for wall and $_A$ for adaptive. The P_W and Q_W can be determined only by geometric constraints, while P_A and Q_A are affected by flow solutions.

Gird Control near Wall :

To control the grid near the wall two constraints (Sorenson, 1980) are imposed. They are orthogonality and the first grid spacing from the wall

$$z_\eta z_\zeta + y_\eta y_\zeta|_w = 0 \tag{19}$$

$$(z_\zeta^2 + y_\zeta^2)^{1/2}|_w \equiv \Delta_{s1} = \text{specified} \tag{20}$$

where $\Delta\eta = \Delta\zeta = 1$ as usual and Δ_{s1} is the first grid spacing from the wall. Except for $z_{\zeta\zeta}$ and $y_{\zeta\zeta}$ at the wall all the other necessary derivatives can be determined if the inner wall boundary are specified. The second derivatives in ζ are approximated by using the one-sided differences which contain previous iteration values. The source terms are assumed to have following forms.

$$P_W(\eta,\zeta) = p(\eta)\, e^{-a\zeta}, \quad Q_W(\eta,\zeta) = q(\eta)\, e^{-b\zeta} \tag{21}$$

The above constraints can decide the $p(\eta)$, $q(\eta)$, and the parameters, a and b, are specified. If a larger value of a or b is used, the effect of constraints decays very quickly. On the other hand it decays slowly for a smaller value. In solving the set of equations, the Successive Line Over-Relaxation (SLOR) method is utilized. Near the sharp corners, numerical instability may often occur. To remedy this problem, various methods including under relaxation and mixed finite difference schemes based on the sign of P and Q are used.

Adaptive Gird :

To improve the resolution in regions where rapid flow variations occur and/or to reduce the global error, an adaptive grid may be utilized. The basic idea of adaptive grid which provides automatic adjustment to the flow pattern can be obtained by equidistribution principle, which for 1-D case can be expressed by

$$x_\eta w = (\Delta x)\, w = \text{const} \tag{22}$$

This means simply that the mesh size is smaller when a weight function w is large and vice versa. If we differentiate it once with respect to η and compare with the Poisson elliptic grid generating equation for 1-D, it can be easily seen that the control function P is related to $\frac{1}{w}\frac{\partial w}{\partial \eta}$. The control functions (Thomas, Middlecoff, 1980) are introduced by

$$P_A = (\eta_x^2 + \eta_y^2)\,\phi(\eta,\zeta), \quad Q_A = (\zeta_x^2 + \zeta_y^2)\,\phi(\eta,\zeta) \tag{23}$$

Anderson (Anderson, 1987) related these ϕ and ψ to the weight function w as

$$\phi = \frac{1}{w}\frac{\partial w}{\partial \eta}, \quad \psi = \frac{1}{w}\frac{\partial w}{\partial \zeta} \tag{24}$$

In this study w is determined based on the pressure gradient as

$$w = 1 + A|\nabla p|/|\nabla p|_{max} \tag{25}$$

where A is a constant and the number 1 is introduced to avoid infinite grid spacing in regions where the pressure gradient vanishes. The pressure gradient in Eq. (25) can be obtained by

$$\frac{\partial p}{\partial z} = (y_\zeta \frac{\partial p}{\partial \eta} - y_\eta \frac{\partial p}{\partial \zeta})/\sqrt{g}$$

$$\frac{\partial p}{\partial y} = (-z_\zeta \frac{\partial p}{\partial \eta} + z_\eta \frac{\partial p}{\partial \zeta})/\sqrt{g} \tag{26}$$

where $\sqrt{g} = \frac{1}{J}$. Note that the pressure obtained by numerical integration is defined at cell center points and thus it is necessary to express it at primary grid points before calculating pressure gradients. If we use the weight function based on the above definition directly, then the grid might become rough. Thus, we adapt the following smoothing

$$\bar{w}(k,l) = \frac{1}{16}\{4w(k,l) + 2w(k,l+1) + 2w(k+1,l) + 2w(k-1,l) + 2w(k,l-1) + w(k-1,l-1) + w(k-1,l+1) + w(k+1,l-1) + w(k+1,l+1)\} \tag{27}$$

Since the source terms are defined by Eqs. (21), (23), the Poisson equations are set up as

$$a\vec{r}_{\eta\eta} - 2\beta\vec{r}_{\eta\zeta} + \gamma\vec{r}_{\zeta\zeta} = -\left\{\left[\frac{1}{J^2}p(\eta)\, e^{-a\zeta} + a\phi(\eta,\zeta)\right]\vec{r}_\eta + \left[\frac{1}{J^2}q(\eta)\, e^{-b\zeta} + \gamma\psi(\eta,\zeta)\right]\vec{r}_\zeta\right\} \tag{28}$$

where $\vec{r} = (z, y)^T$. The Eq. (28) is the final form which is numerically solved to get a desired elliptic grid for a waverider. So far we described only 2-D grid, while the porblem is 3-D. We can easily construct the desired 3-D gird through contraction or expansion of the generated 2-D grid, since the elliptic-cone waverider has a conical shape. Since the $\xi =$ constant plane is perpendicular to the x-axis, for the grid constructed here we have

$$\xi_y = \xi_z = 0 \tag{29}$$

4.3 Redistribution of Boundary Points

The inner and outer boundary points around the tip are redistributed by using Roberts' stretching (Anderson, Tannehill, Pletcher, 1984) which is more desirable than an exponential stretching, since for the region where the clustering is not wanted we can get more uniform stretching. The are length S is defined by

$$S = \frac{(\beta+1) - (\beta-1)\left(\frac{\beta+1}{\beta-1}\right)^{1-\bar{\zeta}}}{1 + \left(\frac{\beta+1}{\beta-1}\right)^{1-\bar{\zeta}}} S_t \tag{30}$$

where $0 < \beta < \infty$ and $\bar{\zeta} = \frac{1}{\zeta_{max} - 1}$. As $\beta \to 0$, more clustered grid near $S=0$ can be obtained. As $\beta \to \infty$, it becomes uniform. Based on the arc lengths we can get the clustered grid as we like. This is done by redistributing the x and y coordinates along the wall line by means of the interpolation according to the calculated arc lengths.

5. DISCUSSIONS

Fig. 2 shows pressure contours normalized by the freestream pressure of the waverider flow at $M_\infty = 3$ with no incidence. It can be seen clearly that the shock stands off from the leading edge, which is different from the shock position at the idealized on-design condition.

Figs. 3~6 show various plots for the waverider flowfield at $M_\infty = 10$ with no incidence. In Fig. 3 the disturbed-velocity distribution on the plane perpendicular to the x-axis is depicted. The disturbance is limited to a small region below the waverider, and a bow shock is captured very close to the waverider compression surface. It should be noted that near the tip region, a λ-shock is developed. It can be seen more distinctly by the stagnation pressure contours shown in Fig. 4. A schematic diagram of the λ-shock pattern is shown in Fig. 5. The oblique shock from the tip is quite strong, since the

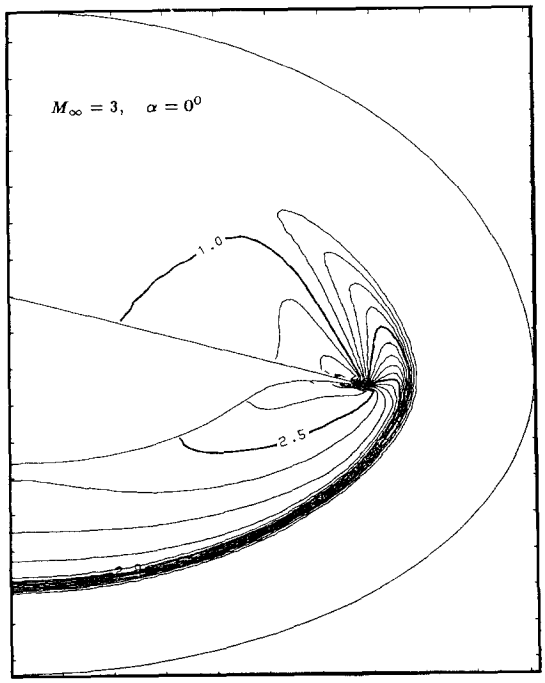

Fig. 2 Pressure contours

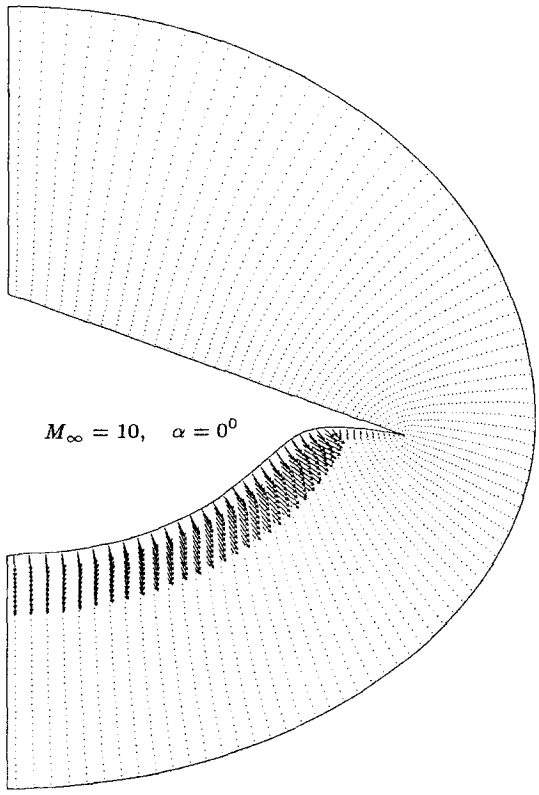

Fig. 3 Cross-plane velocity distribution

freestream Mach number is a quite large value of 10. Fig. 6 shows the wall pressure distribution. The rapid pressure jump on the lower surface occurs across the Mach-stem portion of the lambda shock that is normal to the surface. The upper surface has the undisturbed freestream value.

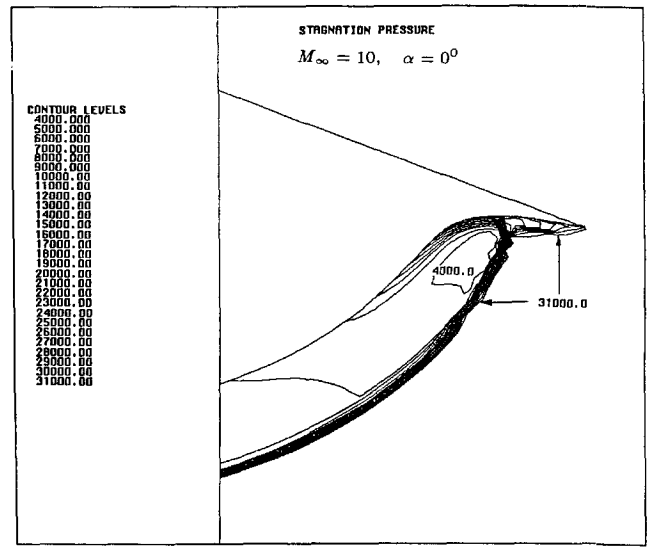

Fig. 4 Total pressure contours

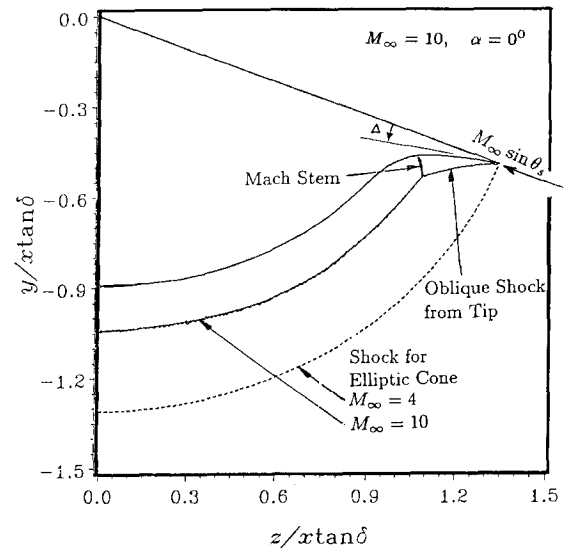

Fig. 5 Schematic diagram of lambda shock

Figs. 7, 8 show a couple of plots at various freestream Mach numbers M_∞=3, 4, 4, 5, and 5 with the fixed angle of attack α=0°. Fig. 7 compares the pressure distribution in the shock layer near the lower symmetry plane. It can be seen that as M_∞ increases, the shock strength increases and the shock location moves toward the body.

Fig. 8 compares the wall pressure distributions. The wall pressure for the upper waverider surface does not change so much except for the case of the Mach number below the on-design value. This implies that the upper freestream surface remains undisturbed for the higher Mach numbers above the on-design value. Especially at M_∞=4.5 the pressure variation near the tip resembles that of the Hypersonic Small Disturbance Theory (HSDT) prediction and the waverider upper surface has the freestream pressure. The wall pressure for the lower compression surface increases as the Mach number increases except for the leading edge region.

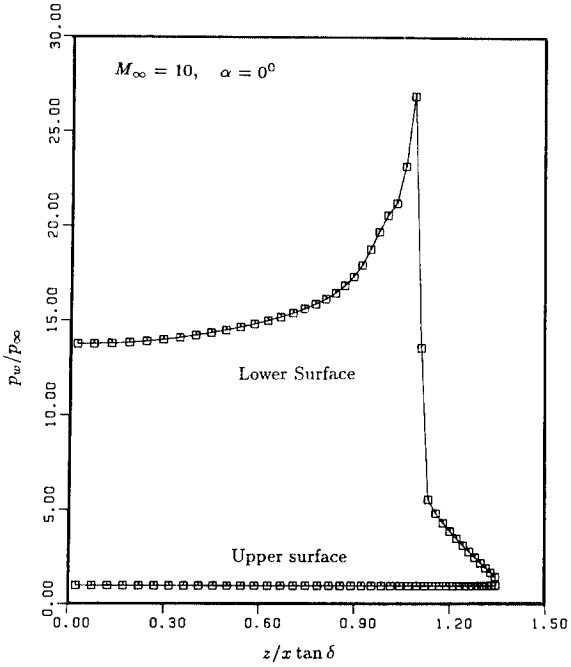

Fig. 6 Wall pressure distribution

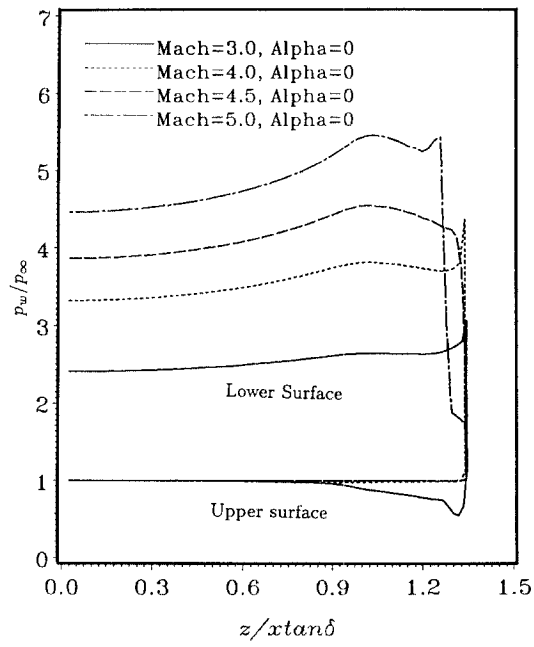

Fig. 8 Wall pressure

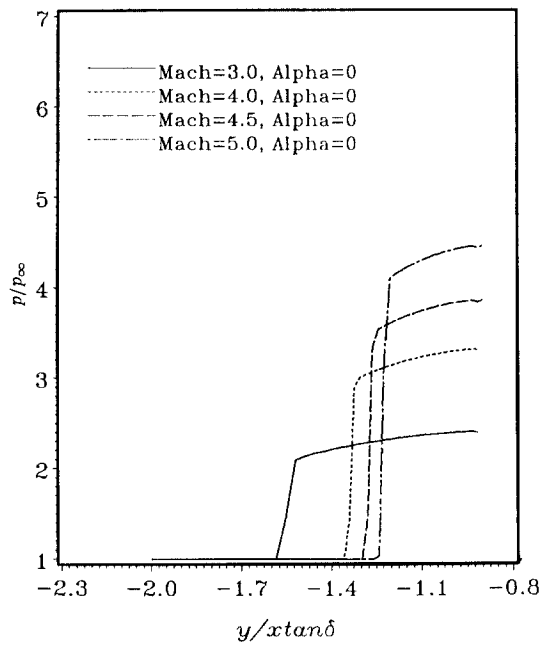

Fig. 7 Pressure near lower symmetry plane

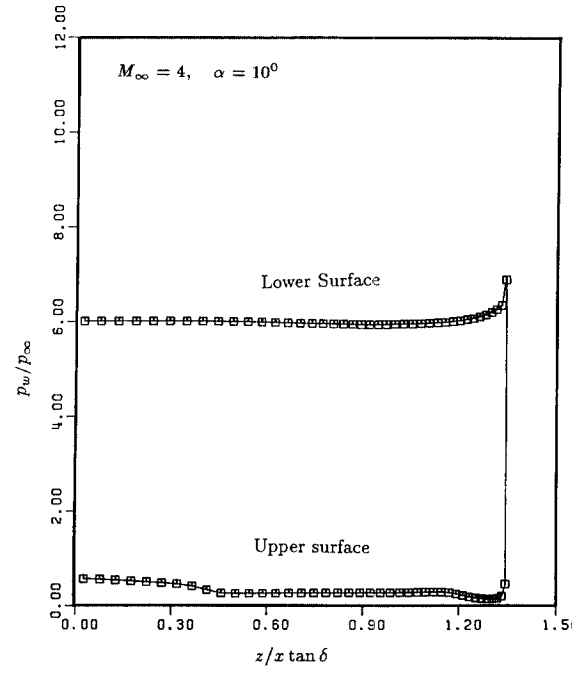

Fig. 9 Wall pressure distribution

Figs. 9, 10 are a couple of plots for the waverider flowfield at $M_\infty=4$ and $\alpha=+10^\circ$. The wall pressure is shown in Fig. 9. We can see that the cross flow around the leading edge affects the upper part of the waverider forcibly. In Fig. 10 the azimuthal velocity shows a positive peak value which indicates the accelerated cross flow at the leading edge. The azimuthal velocity w, normalized by the freestream speed V_∞, should be zero on the waverider upper surface. The w in the figure shows the values for the half grid spacing off from the wall. A small discontinuity is detected at $\eta \cong 75$. This corresponds to the pressure-rise point near the upper waverider surface at $z/x \tan\delta \cong 0.4$ in Fig. 9.

Figs. 11, 12 are a couple of plots for the waverider flowfield at $M_\infty=4$ and $\alpha=-8^\circ$. Fig. 11 shows the stagnation pressure contours. We can see the development of the upper and lower shocks. The shock below the waverider has a stronger strength near the tip area, and it becomes weaker as it approaches the lower symmetry plane. The shock above the waverider is nearly attached at the tip and weakeus as it approaches the upper symmetry plane. In Fig. 12 we can see the two areas delineated by the difference between the upper and lower wall pressures have approximately the same size.

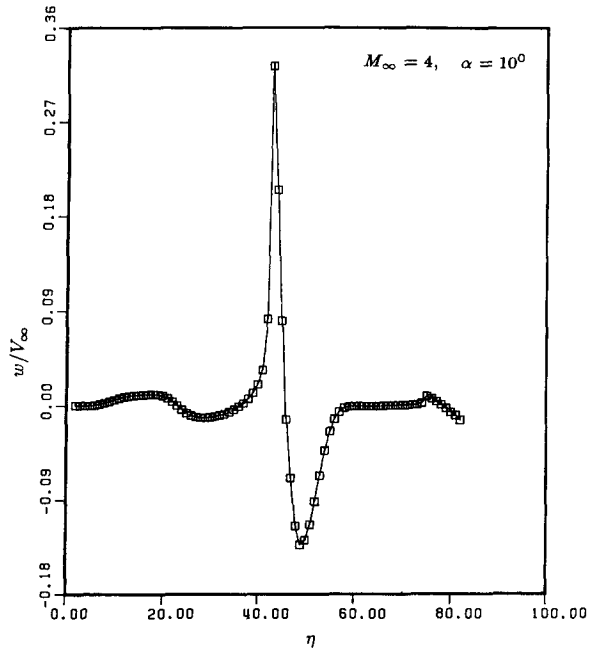

Fig. 10 Azimuthal velocity component

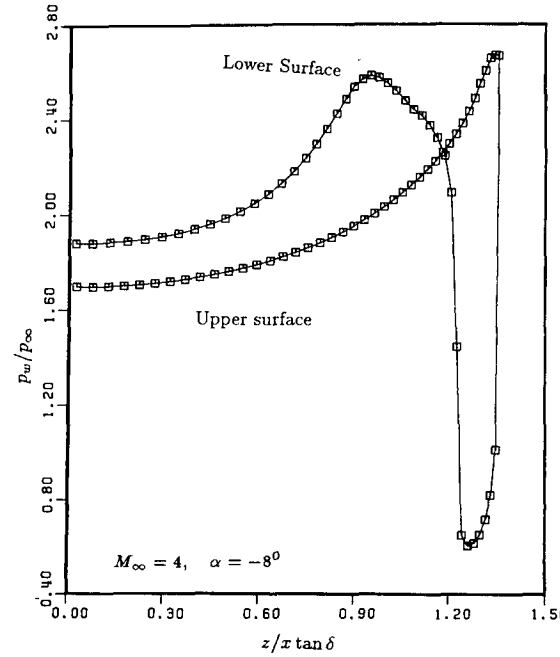

Fig. 12 Wall pressure distribution

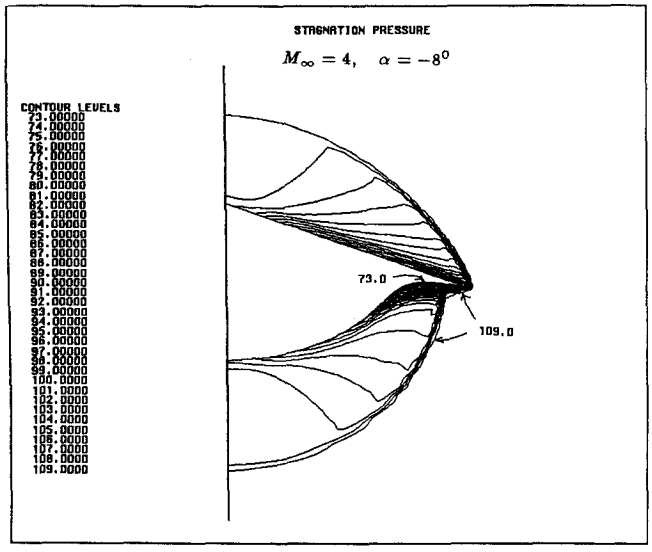

Fig. 11 Total pressure contours

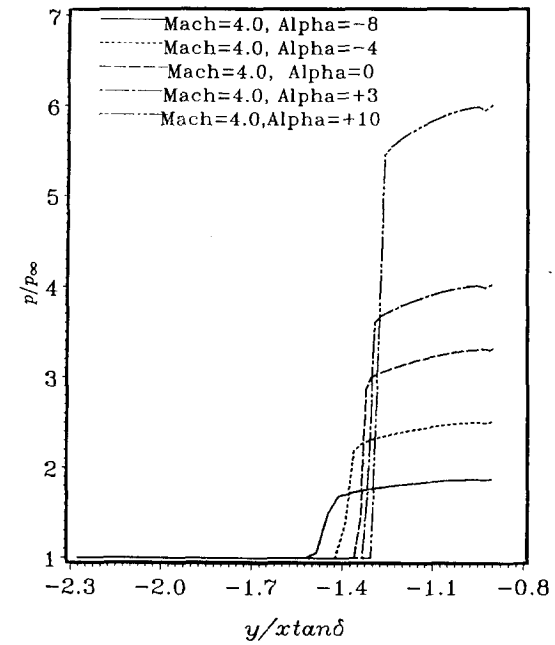

Fig. 13 Pressure near lower symmetry plane

This implies that the lift is almost zero.

Figs. 13, 14 show the comparisons of the pressure distributions at various angles of attack $\alpha = -8^\circ, -4^\circ, 0^\circ, +3^\circ, +10^\circ$ with freestream Mach number fixed at $M_\infty = 4$. Fig. 13 compares the pressure distribution and shock locations near the lower symmetry plane. It can be seen that as α increases, the shock strength increases and the shock moves toward the body. In this respect the effect of the increasing α is similar to that of the increasing M_∞ as can be seen in Fig. 7. Fig. 14 compares the wall pressure distributions. For the negative angles of attack the pressure lines for the lower waverider surface intersect those for the upper waverider surface. The areas of the left hand side of the intersection denote positive lift and the areas of the right hand side denote negative lift. This explains the lift decreasing at negative angles of attack. At the positive angles of attack the pressure near the upper symmetry plane becomes higher than that near the tip region, because a weak imbedded shock develops on the upper surface. We can also see the pressure near the lower symmetry plane increase in comparison with the tip region, as α increases. This is because the flow deflection near the symmetry plane due to the high angle of attack is greater than the flow deflection due to the perturbed elliptic cone near the major axis, as α increases.

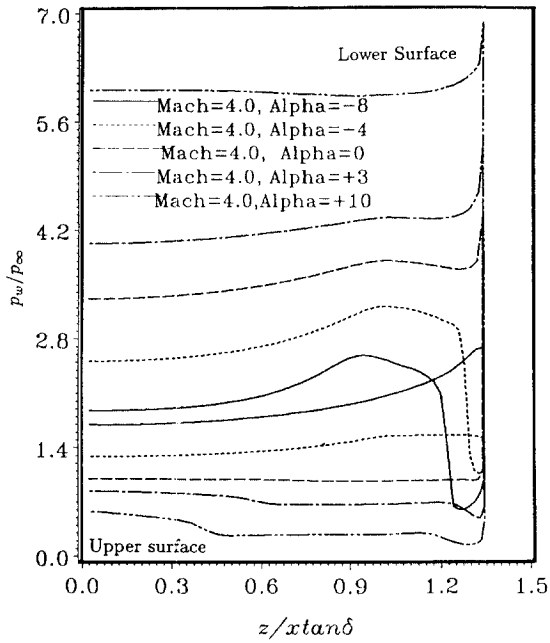

Fig. 14 Wall pressure

6. CONCLUSIONS

The great importance for the CFD calculations is associated with the off-design results. At $\alpha=0^\circ$ and for $M_\infty>4$, the bow shock fits more tightly under the waverider body. Near the leadinge-edge of the waverider, a λ-type shock configuration appears to develop. This becomes more pronounced as M_∞ increases, the largest value being $M_\infty=10$ in this study. This is a new effect that was not known from previous studies. The λ-shock configuration occurs for other off-design conditions also as part of the adjustment of the main conical bow shock to the local leading-edge conditions.

For $M_\infty=3$ and $\alpha=0^\circ$, the bow shock stands off from the body, the more so as M_∞ decreases. There is then a flow in the gap between the shock and the leading edge as the flow adjusts to the higher pressure under the body to the lower pressure on top.

When the angle of attack is positive ($\alpha>0^\circ$) the shock tends to fit tighter to the lower compression surface, and there is an expansion region over the upper surface. A very weak shock develops on the upper surface. This is needed to deflect the flow that has expanded over the leading edge back parallel to the vertical symmetry plane. For negative angles of attack, the shock below the body weakens and a bow shock develops over the upper surface of the body.

ACKNOWLEDGMENT

This work was supported by NASA Langley Grant No. NAG-1-886. The author really appreciate the support.

REFERENCES

Anderson, D.A., 1987, "Equidistribution Schemes, Poisson Generators, and Adaptive Grids," Applied Mathematics and Computation, Vol.24, pp. 211~227.

Anderosn, D.A., Tannehill, J.C. and Pletcher, R.H., 1984, "Computational Fluid Mechanics and Heat Transfer," McGraw-Hill.

Chakravarthy, S.R. and Osher, S., 1985, "A New Class of High Accuracy TVD Schemes for Hyperbolic Conservation Laws," AIAA Paper 85-0363.

Chakravarthy, S.R., Szema, K-Y., Goldberg, U.C., Gorski, J. J. and Osher, S. 1985, "Application of a New Class of High Accuracy TVD Schemes to the Navier-Stokes Equations," AIAA Paper 85-0165.

Harten, A., 1983, "High Resolution Schemes for Hyperbolic Conservation Laws," J. of Computational Physics, Vol.49, pp. 357~393.

Jischke, M.C., Rasmussen, M.L. and Daniel, D.C., 1983, "Experimental Surface Pressures on Cone-Derived Waveriders for $M_\infty=3-5$," Journal of Spacecraft and Rockets, Vol. 20, No.6, pp. 539~545.

Jones, K.D. and Dougherty, F.C., 1990, "Computational Simulation of Flows about Hypersonic Geometries with Sharp Leading Edges," AIAA Paper 90-3065-CP, 8th Applied Aerodynamics Conference, Aug. 20~22, Portland, Oregon.

Jones, K.M., 1986, "Application of a Supersonic Full Potential Method for Analysis of Waverider Configurations," NASA Technical Paper 2608.

Lawrence, S.L., Tannehill, J.C. and Chaussee, D.S., 1986, "An Upwind Algorithm for the Parabolized Navier-Stokes Equations," AIAA Paper and 86-1117.

Liao, J.R., Isaac, K. M. and Miles, J. B., 1990, "Navier-Stokes Simulation of Waverider Flowfields," AIAA Paper 90-3066-CP, 8th Applied Aerodynamics Conference, Aug. 20~22, Portland, Oregon.

Long, L.N., 1990, "Off-Design Performance of Hypersonic Waveriders," J. of Aircraft, Vol.27, No.7.

Rasmussen, M.L., Jischke, M.C. and Daniel, D.C., 1982, "Experimental Forces and Moments on Cone-Derived Waveriders for $M_\infty=3$ to 5," Journal of Spacecraft and Rockets, Vol.19, No.6, pp. 592~598.

Roe, P.L., 1981, "Approximate Riemann Solvers, Parameter Vectors, and Difference Schemes," J. of Computational Physics, Vol. 43, pp. 357~372.

Sorenson, R.L., 1980, "A Computer Program to Generate Two-Dimensional Grids About Airfoils and Other Shapes by the Use of Poisson's Equation," NASA TM-81198.

Thomas, P.D. and Middlecoff, J.F., 1980, "Direct Control of the Grid Point Distribution in Meshes Generated by Elliptic Equations," AIAA J., Vol.18, No.6, pp. 652~656.

Thompson, J.F., Lijewski, L.E. and Gatlin, B., 1989, "Efficient Application Techniques of the EAGLE Grid Code to Complex Missile Configurations," AIAA Paper 89-0361, 27th Aerospace Sciences Meeting Jan, 9~12, Reno, Nevada.

van Leer, B., 1982, "Flux-Vector Splitting for the Euler Equations," Lecture Notes in physics, Vol.170, pp. 507~512.

Warming, R.F., Beam, R.M. and Hyett, B.J., 1975, "Diagonalization and Simultaneous Symmetrization of the Gas-Dynamic Matrices," Mathematics of Computation, Vol. 29, No. 132, pp. 1037~1045.

Yee, H.C. and Harten, A., 1987, "Implicit TVD Schemes for Hyperbolic Conservation Laws in Curvilinear Coordinates," AIAA J., Vol.25, No. 2, pp. 266~274.

Yoon, B.H., 1992, "On-design Solutions of Hypersonic Flows past Elliptic-Cone Derived Waveriders," KSME Journal, Vol.6, No.1, pp. 24~30.